



HAL
open science

Characterization of HD 206893 B from Near- to Thermal-infrared

Tiffany Meshkat, Peter Gao, Eve Lee, Dimitri Mawet, Elodie Choquet, Marie Ygouf, Rahul Patel, Garreth Ruane, Jason Wang, Nicole Wallack, et al.

► **To cite this version:**

Tiffany Meshkat, Peter Gao, Eve Lee, Dimitri Mawet, Elodie Choquet, et al.. Characterization of HD 206893 B from Near- to Thermal-infrared. *The Astrophysical Journal*, 2021, 917 (2), pp.62. 10.3847/1538-4357/ac09ed . hal-03582372

HAL Id: hal-03582372

<https://amu.hal.science/hal-03582372>

Submitted on 6 Dec 2022

HAL is a multi-disciplinary open access archive for the deposit and dissemination of scientific research documents, whether they are published or not. The documents may come from teaching and research institutions in France or abroad, or from public or private research centers.

L'archive ouverte pluridisciplinaire **HAL**, est destinée au dépôt et à la diffusion de documents scientifiques de niveau recherche, publiés ou non, émanant des établissements d'enseignement et de recherche français ou étrangers, des laboratoires publics ou privés.

3 CHARACTERIZATION OF HD 206893 B FROM NEAR TO THERMAL INFRARED

4 TIFFANY MESHKAT¹, PETER GAO^{2,*}, EVE J. LEE³, DIMITRI MAWET^{4,6}, ELODIE CHOQUET⁵, MARIE YGOUF⁶, RAHUL PATEL¹,
5 GARRETH RUANE⁶, JASON WANG^{4,†}, NICOLE WALLACK⁷, OLIVIER ABSIL^{8,‡}, CHARLES BEICHMAN^{1,6}

Draft version April 15, 2021

6 ABSTRACT

7 HD 206893 B is a brown dwarf companion orbiting inside the debris disk of its host star. We detect the
8 brown dwarf in *Ms*-band using the Keck/NIRC2 instrument and vortex coronagraph. We measure
9 its magnitude to be $M_s = 12.97_{-0.11}^{+0.10}$. It is at an angular separation of 0.22 ± 0.03 arcsec, and a
10 position angle (PA) of 39.6 ± 5.4 deg East of North. Using this *Ms*-band measurement **and the**
11 **system age**, we use three evolutionary models to estimate the mass to be **12-78** M_{Jup} . We analyze
12 the atmospheric properties from 1 to 5 microns using a grid of simulated atmospheric models. We find
13 that a sedimentation flux f_{sed} value ~ 0.2 provides the best fit to the data, suggesting high vertically
14 extended clouds. This may be indicative of high altitude grains or a circumplanetary disk. **Our**
15 **model radii and luminosities for the companion find the best-fits are ages of <100 Myr**
16 **and masses <20** M_{Jup} , **consistent with our mass estimate from the evolutionary models**
17 **using the *Ms*-band data alone.** We detect orbital motion of the brown dwarf around the host
18 star in comparison to the discovery image and derive orbital parameters. Finally we analyze how
19 the companion brown dwarf interacts with the debris disk by estimating the location of the chaotic
20 zone around the brown dwarf **using values derived from this study's estimated mass and**
21 **orbital constraints.** We find that the collisions within the debris belt are likely driven by secular
22 perturbations from the brown dwarf, rather than self-stirring.

23 *Keywords:* stars: individual (HD 206893 B)—planets and satellites: detection — circumstellar material

24 1. INTRODUCTION

25 HD 206893 is a bright ($H = 5.69$), nearby (40.77 ± 0.05
26 **pc; Gaia EDR3**), F5V star with a **an unresolved debris disk, inferred by its infrared excess (Moór et al.**
27 **2006).** Milli et al. (2017) reported the detection of a
28 low mass companion at a projected separation of
29 ~ 10 au, inside the debris disk belt with an inner edge of
30 ~ 50 au. The companion was first detected in *H*-band
31 with IRDIS on SPHERE/VLT, with a $H = 16.79 \pm 0.06$
32 mag. The team confirmed the companion is co-moving
33 with follow-up NACO/VLT observations in *L'*-band and
34 finds a magnitude of $13.43_{-0.15}^{+0.17}$. The age for the star is
35 not well constrained, as it is not a member of a mov-
36 ing group. The age ranges from 200 Myr (Zuckerman
37 & Song 2004) up to 2.1 Gyr (David et al. 2016). Using
38 the AMES-Cond model (Baraffe et al. 2003) **and the**
39

40 **assumed system age range of 0.2 to 2 Gyr,** Milli
41 et al. found the mass of the companion to be 24-75
42 M_{Jup} . In comparison to young bound and field compan-
43 ions, they found that HD 206893 B is one of the reddest
44 late-L dwarfs, likely due to a dusty atmosphere. They
45 concluded that the companion is likely orbiting interior
46 to and in the same plane as the debris disk. This is only
47 the second brown dwarf companion discovered inside a
48 debris disk gap, following the discovery of HR 2562 B
49 (Konopacky et al. 2016).

50 Delorme et al. (2017) characterized the companion
51 with spectral data from the integral field spectrograph
52 (IFS) on SPHERE/VLT, providing spectral coverage
53 from 0.95-1.63 μm with a resolution of $R=30$. These ob-
54 servations were obtained in dual-band imaging, thus K1
55 ($2.110\mu\text{m}$) and K2-band ($2.251\mu\text{m}$) imaging data were
56 simultaneously obtained with the IFS data. Using a
57 range of age identifiers applied to derive the host star
58 properties (color-magnitude position, lithium and bar-
59 ium abundances, rotation rate, **X-ray, chromospheric**
60 **emission, and potential moving group associa-**
61 **tion), they adopted the age of 250_{-200}^{+450} Myr. The error**
62 **on the age of the star is large due to its spec-**
63 **tral type.** They compared the spectral energy distri-
64 bution (SED) of the companion to a grid of BT-Settl
65 (Allard 2014) models as well as Exoplanet Radiative-
66 convective Equilibrium Model (ExoREM; Baudino et al.
67 2015) model atmospheres. They found the best fit is a
68 companion with a very dusty atmosphere, $T_{\text{eff}} = 1300$ K,
69 and $\log g = 4.4$ to 4.8, **consistent with a late L spec-**
70 **tral type.** They also found that the companion alone
71 cannot be responsible for the shape of the inner edge of
72 the debris disk, and suggested there may be additional,
73 unseen lower mass companions in the system.

¹ IPAC, California Institute of Technology, M/C 100-22, 1200 East California Boulevard, Pasadena, CA 91125, USA

² Department of Astronomy and Astrophysics, University of California, Santa Cruz, Santa Cruz, CA 95064, USA

³ Department of Physics and McGill Space Institute, McGill University, 3550 rue University, Montreal, QC, H3A 2T8, Canada

⁴ Department of Astronomy, California Institute of Technology, 1200 East California Boulevard, Pasadena, CA 91125, USA

⁵ Aix Marseille Univ, CNRS, CNES, LAM, Marseille, France

⁶ Jet Propulsion Laboratory, California Institute of Technology, 4800 Oak Grove Drive, Pasadena, CA 91109, USA

⁷ Division of Geological & Planetary Sciences, California Institute of Technology, Pasadena, CA 91125, USA

⁸ Space sciences, Technologies, and Astrophysics Research (STAR) Institute, Université de Liège, 19c allée du Six Août, B-4000 Sart Tilman, Belgium

* NHFP Sagan Fellow

† 51 Pegasi b Fellow

‡ F.R.S.-FNRS Research Associate

Grandjean et al. (2019) combined radial velocity, direct imaging and astrometry data to place limits on the properties of HD 206893 B. In addition to new constraints on the brown dwarf, they **observed** a radial velocity drift which was inconsistent with the brown dwarf **at its projected separation of ~ 11 au.** They **suggested** that an additional inner (1.4-2.6 au), massive ($\sim 15M_{\text{Jup}}$) companion could explain the radial velocity drift. **Both of these companions are internal to the debris disk, which has an inner edge of ~ 50 au.**

Stolker et al. (2020) performed the first photometric analysis of the brown dwarf in M' -band with the NACO instrument at the Very Large Telescope (VLT). **They found that using a $H - L'$ color-magnitude diagram, the brown dwarf appears less red and consistent with low-gravity objects. However, the brown dwarf appears very red on the $L' - M'$ color-magnitude diagram, inconsistent with field dwarfs by 2σ .** They **suggested** the very red color of the brown dwarf is likely due to enhanced cloud density **in the atmosphere, or circumplanetary material.**

Ward-Duong et al. (2020) obtained spectra on the brown dwarf with the Gemini Planet Imager in J , H , $K1$, and $K2$. The shape of the spectra **implied** low surface gravity. They **found** that fitting models to the individual bands produced more internally consistent fits than fitting across the full spectral coverage. The analysis from Stolker et al. (2020) and Ward-Duong et al. (2020) **confirmed** that the brown dwarf is redder than other field dwarfs with similar spectral types. Using ALMA data, Marino et al. (2020) **found** that the debris disk surrounding the host HD 206893, external to the brown dwarf, is comprised of two spatially separated belts of dust.

In this work, we present our detection of HD 206893 B in Ms -band with the vortex coronagraph on the NIRC2 instrument on Keck. In Section 2 we discuss the Ms -band NIRC2 observations and data reduction. In Section 3 we discuss the photometry and astrometry of the companion.

2. OBSERVATIONS AND DATA REDUCTION

HD 206893 was observed on UT 2018 September 24 in Ms -band ($4.670\mu m$) with the NIRC2 instrument on the Keck telescope. Data were obtained with the vortex coronagraph (Serabyn et al. 2017) in order to minimize the flux from the primary star. Each frame had an exposure time of 0.5 s with 60 coadds for a total of 90 frames and 2700 s total exposure time. Before each set of 25 science frames, three calibration frames are taken. These calibration frames include a sky frame for the science data, an image of the unobscured star at a shorter integration time (0.01 s) to be used as a point spread function (PSF) reference, and a sky frame for that PSF reference. Data were obtained as part of an on-going survey targeting stars with debris disks searching for giant planets with deep NIRC2 observations (PI Mawet).

Observations were taken in vertical angle mode in order to allow angular differential imaging (ADI; Marois et al. 2006), which provides speckle diversity to be used in post-processing algorithms. 47° of field rotation was achieved between the first and last frame. Data were obtained in very good seeing conditions, with an average

DIMM of $0''.5$.

The quadrant analysis of coronagraphic images for tip-tilt sensing (QACITS; Huby et al. 2017) was used to keep the primary star well centered behind the vortex coronagraph to minimize stellar flux leakage into the image.

Data were processed using the NIRC2 pre-processing pipeline¹², which has been designed specifically to do pre-processing on NIRC2 vortex data. First the frames are centered to the vortex position. The sky frames are subtracted from both the science and PSF reference data. The frames are then corrected for flat-fielding effects and bad pixels. Finally, the frames are recentered based on the speckle locations, as the star is never perfectly centered behind the coronagraph in each frame. **The distortion is corrected using the NIRC2 solution (Service et al. 2016), with the pixel scale of 0.009942 arcsec/pixel.**

In order to optimally subtract the stellar PSF to reveal the brown dwarf companion, we use the Vortex Image Processing package (VIP; Gomez Gonzalez et al. 2017). The VIP package is used after the data are pre-processed with the NIRC2 pipeline. We use the principal component analysis (PCA; Soummer et al. 2012; Amara & Quanz 2012) algorithm within VIP which calculates the optimal number of principal components to maximize the signal-to-noise of a point source at a specified location. The optimal number of components for our data is four principal components. Due to uncertainty in the exact position of the host star behind the coronagraph, we perform a grid search of small subpixel to pixel shifts of the center of the star and optimize the star center where the brown dwarf signal-to-noise is maximized. The brown dwarf is clearly detected with a signal-to-noise of 11 to the North East of the star (Figure 1). The signal-to-noise includes small sample statistics (Mawet et al. 2014) **to take into account the smaller number of resolution elements at small separation angles.** The image has been smoothed with a kernel the size of the full-width half max (FWHM) to emphasize point sources, since the Ms -band data is oversampled. We do not detect any additional companions in the system. The potential inner companion inferred from radial velocity drift by Grandjean et al. (2019) is inside our inner working angle at the suggested separation (~ 50 mas).

To extract the astrometry and photometry of the brown dwarf, we inject a fake negative companion at an initial approximate location, and use the downhill simplex method to determine the position and flux that minimize the residuals in the final image. The position and flux is adjusted within a predetermined range and the values which minimize chi-squared are the astrometry and photometry. In order to measure the error on these measurements, we inject a fake companion at six different positions with known radii, position angles, and flux in the data, where the brown dwarf has been subtracted away using the position and flux determined above.

We find that the brown dwarf has an $Ms = 12.97_{-0.11}^{+0.10}$, an angular separation of 0.22 ± 0.03 arcsec, and a position angle (PA) of 39.6 ± 5.4 deg East of North. This is consistent with Stolker et al. (2020) photometry and astrometry of the companion in M -band data, which were also obtained in 2018.

¹² https://github.com/vortex-exoplanet/NIRC2_Preprocessing

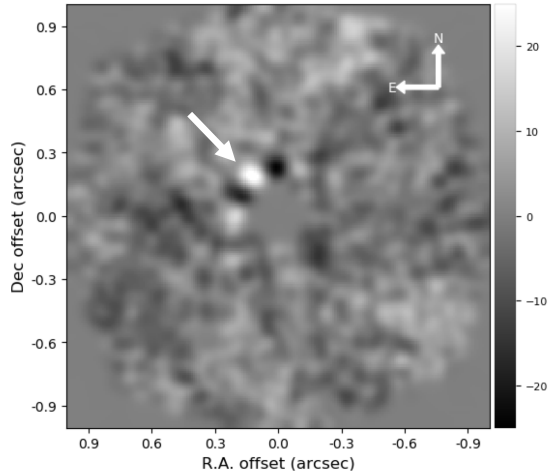


Figure 1. Detection image of HD 206893 B in M_s -band using the vortex coronagraph on NIRC2/Keck. The brown dwarf is North East of the primary star indicated by the white arrow. The image has been smoothed by FWHM sized kernel. The image is on a linear scale in counts. The dark lobes around the brown dwarf are artifacts due to the ADI post-processing due to self subtraction.

3. ANALYSIS

3.1. Companion mass from M_s -band Contrast

We estimate the mass of the companion using the average mass from three evolutionary and atmospheric models (Baraffe et al. 2003; Allard et al. 2013; Chabrier et al. 2000) to be **12-78 M_{Jup}** . We use our M_s -band contrast, assume a distance of **40.77 pc** (Gaia Collaboration 2020), and the age range of 250^{+450}_{-200} Myr from Delorme et al. (2017). Our mass range is consistent with the Milli et al. (2017) mass range (24-73 M_{Jup}), though it extends to lower masses as the age range in Delorme et al. (2017) is lower. **The lower end of our mass range**, which uses our M_s -band contrast measurement alone, is consistent with Delorme et al. (2017) (15-30 M_{Jup}) and Ward-Duong et al. (2020) (12-40 M_{Jup}) mass estimate ranges from fitting to evolutionary models.

3.2. Atmospheric properties

We convert the M_s -band detection into flux using the Keck NIRC2 M_s filter zeropoint¹³ (Rodrigo et al. 2012; Rodrigo & Solano 2020) and find $\lambda F_\lambda = 6.9^{+0.6}_{-0.7} \times 10^{-16}$ W m⁻². We analyze the atmospheric properties of the companion by comparing its SED from 1 to 5 microns (Milli et al. 2017; Delorme et al. 2017) to a custom grid of models computed using a 1D thermal structure code to simulate brown dwarf and exoplanet atmospheres (McKay et al. 1989; Marley et al. 1996; Marley & McKay 1999; Fortney et al. 2005, 2008; Saumon & Marley 2008; Morley et al. 2012). The atmospheric thermal structure and composition are assumed to be in radiative-convective-thermochemical equilibrium. Clouds are computed self-consistently with the thermal structure using the framework of Ackerman & Marley (2001), with its vertical and particle size distribution controlled by the sedimentation efficiency parameter, f_{sed} ; larger f_{sed} results in flattened clouds made of larger particles, while smaller f_{sed} results in more vertically extended clouds

made of smaller particles. Vertical mixing of cloud particles is parameterized through eddy diffusion, with the eddy diffusion coefficient, K_{zz} , computed using mixing length theory with a minimum internal flux assumed in the radiative part of the atmosphere (Ackerman & Marley 2001).

We explore ranges of T_{eff} from 1200 to 1600 K in 100 K steps and $\log(g) = 4.0, 4.4,$ and 5.0 , and consider forsterite and iron clouds. This grid covers the parameter space of the best fitting Exo-REM models from Delorme et al. (2017) and extends beyond it to higher and lower temperatures, and lower gravities. We first try to reproduce the Exo-REM model spectra, as it includes a treatment of the Ackerman & Marley (2001) cloud parameterization (Charnay et al. 2018). However, we found that setting $f_{\text{sed}} = 1$, as was done for the Exo-REM models in Delorme et al. (2017), does not result in the same model spectra nor a good fit to the data (red curve in Figure 2). This could be due to model differences in K_{zz} parameterization and how it responds to cloud radiative feedback. The inclusion of clouds tends to increase mixing, and thus K_{zz} , within the cloud due to increased opacity, which leads to a negative feedback effect of decreasing cloud opacity for a fixed f_{sed} . While our model self-consistently computes K_{zz} with the thermal structure, Exo-REM does not (B. Charnay, personal communication), which may explain our lower cloud opacity.

We find that f_{sed} values ~ 0.2 is needed to best fit our model to the data (blue curve in Figure 2; Figure 3, left), a much lower value than those considered in Delorme et al. (2017), indicating highly vertically extended clouds. In addition, the best-fit f_{sed} decreases to ~ 0.1 towards higher temperatures and lower gravities, likely due to the increased atmospheric temperatures leading to lower cloud masses, resulting in the need for more vertically extended clouds to replicate the same observed reddening. Such low f_{sed} values are unusual for substellar objects, which typically possess $f_{\text{sed}} \geq 1$ when fit with our thermal structure model (e.g. Stephens et al. 2009; Marley et al. 2012; Morley et al. 2012; Rajan et al. 2017). On the other hand, it could be evidence for a population of small, high altitude grains that appear to “extend” a more typical set of iron/forsterite cloud layers (Hiranaka et al. 2016). Delorme et al. (2017) and Ward-Duong et al. (2020) both showed that extinction due to sub-micron forsterite particles in the brown dwarf atmosphere could lead to sufficient reddening of its emission spectrum to explain the observations, though they did not take into account the feedback between the sub-micron particles and the atmosphere. A possible source of these sub-micron particles is that the brown dwarf may be accreting dust from the debris belt, populating the atmosphere with small, high altitude grains (Ward-Duong et al. 2020; Marino et al. 2020). In Section 3.4 we show that the brown dwarf likely is responsible for stirring the planetesimals in the debris disk, lending some strength to this scenario. A circumplanetary disk (Zakhozhay et al. 2017), as was suggested by Delorme et al. (2017) and Stolker et al. (2020), is also possible, though recent ALMA observations of the system by Marino et al. (2020) showed no dust around the

¹³ <https://svo.cab.inta-csic.es/main/index.php>

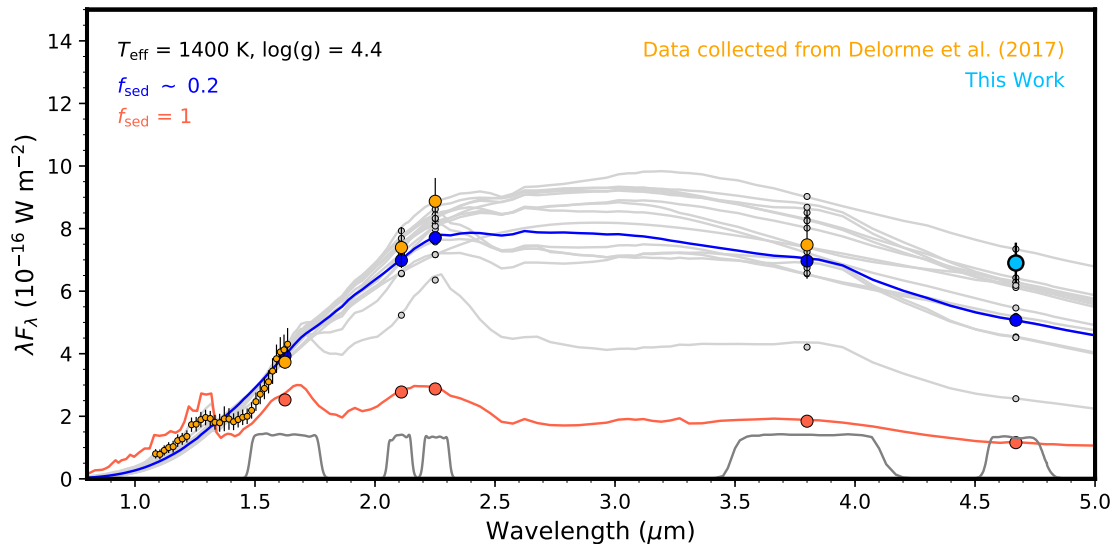


Figure 2. Flux measurements of HD 206893 B across the NIR. The orange points are data presented in Delorme et al. (2017), while the light blue point is our M_s -band observation. Each grey curve shows the best-fit model for each set of T_{eff} and $\log(g)$ in our model grid, all with $f_{\text{sed}} \sim 0.2$. As an example, the dark blue curve shows the model spectrum for the $T_{\text{eff}} = 1400$ K, $\log(g) = 4.4$ case, while the red curve is the corresponding $f_{\text{sed}} = 1$ case. $f_{\text{sed}} \sim 0.2$ models result in a better fit to the data. The grey, red, and dark blue points on the model spectra are the band-integrated model fluxes in each filter.

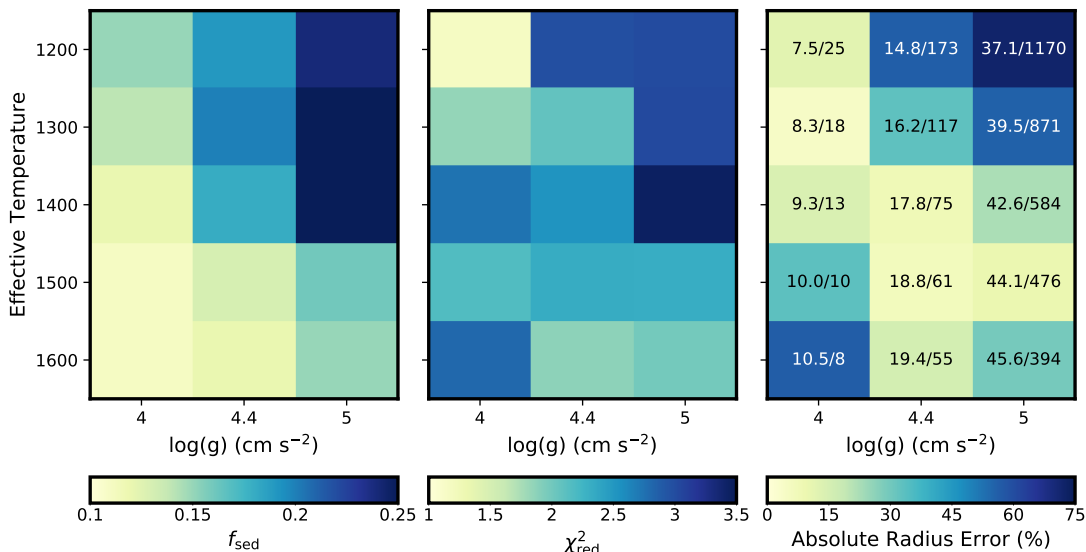


Figure 3. The f_{sed} (left), reduced chi square (middle), and absolute radius error (Equation 1) between the retrieved radii and those predicted by the evolutionary model of Saumon & Marley (2008) (right) for the grid of models we tested. The mass/age of each evolutionary model, in units of M_{Jup}/Myr , are indicated for each model in the radius error plot.

298 brown dwarf, with a dust upper limit of $2 \times 10^4 M_{\oplus}$. 311

299 We are not able to reproduce the water absorption 312
 300 feature at $1.4 \mu m$, as the atmosphere becomes similar to a 313
 301 blackbody due to the low pressures at the photosphere. 314
 302 This sets a lower limit to the reduced χ^2 of most 315
 303 of our model fits to ~ 2 (Figure 3). Interestingly, 316
 304 the $T_{\text{eff}} = 1200$ K and $\log(g) = 4$ model does 317
 305 show a hint of the water feature, resulting in a 318
 306 reduced χ^2 of nearly 1. However, the resulting im- 319
 307 plications for the companion’s mass and age (see 320
 308 Section 3.3) render this result suspect. Instead, 321
 309 we could be seeing numerical instabilities in the 322
 310 cloud treatment at these extreme f_{sed} values. Our 323

311 results are in contrast with those of Delorme et al. 312
 313 (2017), who were able to reproduce the water feature. 314
 315 Though our $f_{\text{sed}} = 1$ models are able to do the same, they 316
 317 are far too dim at longer wavelengths. One possible so- 318
 319 lution is inhomogeneity in the cloud cover (Marley et al. 319
 320 2010; Lew et al. 2016), though it would require the re- 320
 321 maining clouds to be even more optically thick/vertically 321
 322 extended to maintain the extreme redness. In addition, 322
 323 Ward-Duong et al. (2020) observed a drop in flux beyond 323
 2.3 microns with K2 spectra. Our models are not able 324
 to reproduce this significant near-infrared feature along- 325
 side the high L and M_s -band fluxes, suggesting that we 326
 could be missing important details in our model, such as 327

324 absorption longward of 2.3 microns and/or cloud physics
 325 that is not captured by the Ackerman & Marley (2001)
 326 models.

3.3. Evolutionary Models

327
 328 We compare our best-fit radii for the companion to
 329 evolutionary models (Saumon & Marley 2008) to differ-
 330 entiate between the different T_{eff} and $\log(g)$ cases and
 331 to estimate the companion’s age and mass. We define
 332 an absolute radius error between our best-fit radii
 333 R_{fit} and those predicted by the evolutionary mod-
 334 els, R_{evo} , as

$$\text{Absolute Radius Error} = \frac{|R_{\text{evo}} - R_{\text{fit}}|}{R_{\text{evo}}} \quad (1)$$

335 We find that there are multiple models with R_{fit}
 336 and R_{evo} differing by $<10\%$, though in general
 337 models that are either cool and low gravity or
 338 warmer and higher gravity are preferred (Fig-
 339 ure 3). These models in turn imply masses <20
 340 M_{Jup} and ages <100 Myr, within the range derived
 341 by Delorme et al. (2017) and consistent with the mass
 342 estimates range from our M_s -band measurement in Sec-
 343 tion 3.1 (12-78 M_{Jup}). It is also consistent with the
 344 lower mass estimate in Ward-Duong et al. (2020) due
 345 to the peak shaped morphology of the H -band spec-
 346 tra. However, we note that the evolutionary models to
 347 which we have compared were not computed for such
 348 red objects (Saumon & Marley 2008), so age and mass
 349 estimates stemming from such comparisons may not be
 350 reliable. For the subsequent analysis, we take the con-
 351 servative approach and use our derived mass range from
 352 Section 3.1 (12-78 M_{Jup}).

3.4. Astrometry

Table 1
 Astrometry of HD 206893 B.

Observation dates UT	Instrument	Separation (mas)	PA ($^{\circ}$)
2015 Oct 4 ^a	SPHERE/VLT	270.4 \pm 2.6	69.95 \pm 0.55
2016 Aug 8 ^a	NACO/VLT	268.8 \pm 10.4	61.6 \pm 1.9
2016 Sep 16 ^b	SPHERE/VLT	265 \pm 2	62.25 \pm 0.11
2016 Sep 22 ^c	GPI/Gemini	267.6 \pm 2.9	62.72 \pm 0.62
2016 Oct 21 ^c	GPI/Gemini	265.0 \pm 2.7	61.33 \pm 0.64
2017 Jul 14 ^d	SPHERE/VLT	260.3 \pm 2	54.2 \pm 0.4
2017 Nov 09 ^c	GPI/Gemini	256.9 \pm 1.1	51.01 \pm 0.35
2018 Jun 20 ^d	SPHERE/VLT	249.1 \pm 1.6	45.5 \pm 0.4
2018 Jun 08 ^e	NACO/VLT	246.51 \pm 21.34	42.80 \pm 2.24
2018 Sep 24 ^c	GPI/Gemini	251.7 \pm 5.4	42.6 \pm 1.6
2018 Sep 24 ^f	NIRC2/Keck	220 \pm 30	39.6 \pm 5.4

^aMilli et al. (2017)

^bDelorme et al. (2017)

^cWard-Duong et al. (2020)

^dGrandjean et al. (2019)

^eStolker et al. (2020)

^fThis work.

354 The clear M_s -band detection shows significant orbital
 355 motion compared to the data presented in the discovery
 356 paper (Milli et al. 2017). Figure 4 shows the position
 357 of the brown dwarf relative to the host star over several

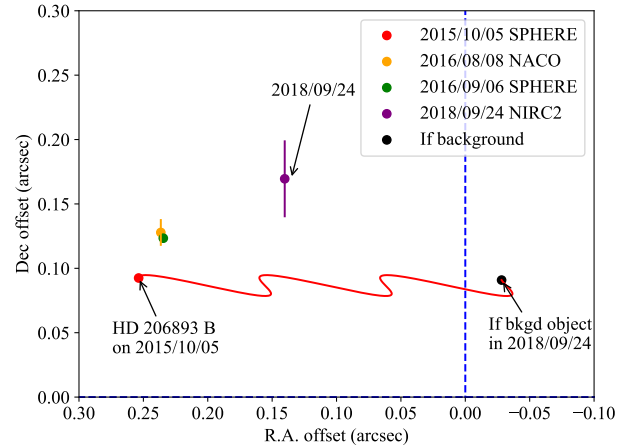


Figure 4. Position of the brown dwarf relative to its host star since 2015. Error bars are included on the plot, though they are small and most are encompassed inside the points.

358 years since the discovery in 2015. The black point in-
 359 dicates the position that the 2015 detected point source
 360 would be if it were a background star, using parallax
 361 and the proper motion of HD 206893. We show that our
 362 2018 M_s -band Keck/NIRC2 detection is not consistent
 363 with a background star and its movement is likely orbital
 364 motion.

365 In order to put constraints on the detected orbital
 366 motion, we input the separation and PA values into the
 367 *orbitize* python package (Blunt et al. 2020; Foreman-
 368 Mackey et al. 2013). We assume a stellar mass of
 369 $1.32 \pm 0.02 M_{\odot}$ (Delorme et al. 2017) and the brown
 370 dwarf mass range derived in this work (12-78
 371 M_{Jup}). This is a total system mass of $1.36 \pm 0.04 M_{\odot}$.
 372 We assume a parallax of 24.53 ± 0.04 mas (Gaia
 373 EDR3). We fit the orbit using Markov Chain Monte
 374 Carlo (MCMC) with 20 temperatures, 100 walkers, 10^6
 375 orbits and 10^5 burn steps.

376 The derived orbital parameters are presented in Table
 377 2. The posterior distributions are shown in the
 378 appendix (see Figure 6). We find that the brown
 379 dwarf has a semi-major axis of $10.6^{+3.7}_{-2.1}$ au. This is con-
 380 sistent with the semi-major axes estimated by Milli
 381 et al. (2017), Delorme et al. (2017), Stolker et al.
 382 (2020), and Ward-Duong et al. (2020). The eccentric-
 383 ity derived in Marino et al. (2020) is consistent
 384 with our eccentricity range.

385 HD 206893 B is located inside the observed debris
 386 belts (Milli et al. 2017; Marino et al. 2020). HD 206893
 387 B is sufficiently far away from the debris belt so its
 388 chaotic zone does not overlap with the belt (vertical
 389 gray box in Figure 5), calculated assuming the chaotic
 390 zone’s inner edge $(1 - 1.17\mu^{0.28})a_{\text{pl}}$ and the outer edge
 391 $(1 + 1.76\mu^{0.31})a_{\text{pl}}$ where μ is the mass ratio between the
 392 brown dwarf and the star, and a_{pl} is the semimajor axis
 393 of the planet (see Morrison & Malhotra 2015, their Table

Table 2
Orbital parameters of HD 206893 B.

Parameter	Posterior 50%±1σ	Unit
Semi-major axis (a)	$10.46^{+1.47}_{-1.93}$	au
Eccentricity (e)	$0.22^{+0.16}_{-0.16}$	–
Inclination (i)	$143.21^{+14.99}_{-5.93}$	°
Argument of Periastron (ω)	$177.3^{+111.8}_{-130.1}$	°
Position angle of nodes (Ω)	$152.3^{+111.1}_{-88.0}$	°
Epoch of Periastron Passage (τ)	$0.28^{+0.44}_{-0.12}$	–

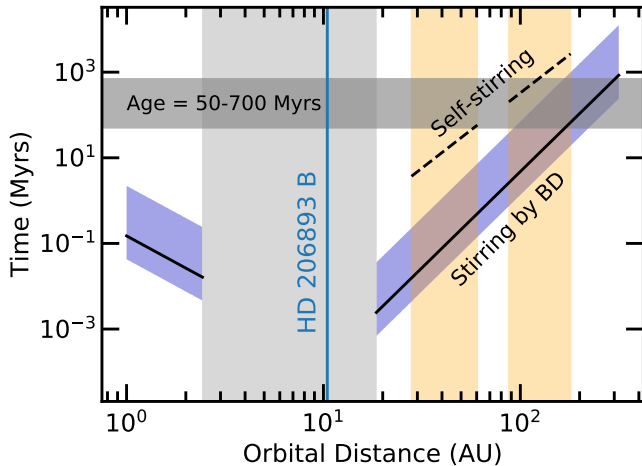


Figure 5. The timescale for HD 206893 B to stir particles at different orbital distances. The thick vertical gray box illustrates the chaotic zone around the orbit of HD 206893 B given the range of masses $12\text{--}78 M_{\text{Jup}}$. The orange box shows the reported width and location of the debris belts (Marino et al. 2020). The horizontal gray line shows the age range of the brown dwarf. The dashed line shows the self-stirring scenario, where the dust are maintained by self-stirring by the planetessimals. The solid black line is the scenario where stirring by the brown dwarf dominates, with a blue outline to indicate the range in both masses and eccentricities (0.22 ± 0.16) of HD 206893 B. Due to the position and relatively high mass of the brown dwarf, the collisions in the debris belt are likely maintained by secular perturbations from HD 206893 B.

for the inner belt, and

$$t_{ss,o} \sim 2.9 \text{ Gyrs} \left(\frac{1.24 M_{\odot}}{M_{\star}} \right)^{0.35} \times \left(\frac{a_{\text{disk}}}{180 \text{ au}} \right)^{3.575} \left(\frac{\Delta a / a_{\text{disk}}}{0.69} \right)^{1.15} \quad (3)$$

for the outer belt, where a_{disk} is the semi-major axis of the planetesimals, M_{\star} is the mass of the host star, and Δa is the width of the debris belts, taken from Marino et al. (2020). Figure 5 demonstrates that the inner belt could be maintained by self-stirring but in the outer belt, t_{ss} is comparable to the age of the system. We note however that if these 1000-km sized bodies can be coagulated before the dispersal of the disk gas, the self-stirring timescale can be dramatically shortened (e.g., Krivov & Booth 2018).

We now consider stirring of the debris belt from secular perturbation by HD 206893 B. The orbit-crossing timescale of two planetesimals as their eccentricities are pumped by the brown dwarf can be approximated as $t_{\text{cross}} \sim 1/Ae_{bd}$ where A is the precession frequency and e_{bd} is the eccentricity of the brown dwarf. We follow Mustill & Wyatt (2009) to compute t_{cross} for particles that are interior and exterior to the brown dwarf, assuming particles were initially on circular orbits:

$$t_{\text{cross}} \approx 2.8 \text{ Myrs} \frac{(1 - e_{bd}^2)^{3/2}}{e_{bd}} \left(\frac{a_{\text{disk}}}{100 \text{ AU}} \right)^{9/2} \times \left(\frac{M_{\star}}{M_{\odot}} \right)^{1/2} \left(\frac{16 M_{\text{Jup}}}{M_{bd}} \right) \left(\frac{10.6 \text{ AU}}{a_{bd}} \right)^3 \quad (4)$$

for particles exterior to the brown dwarf’s orbit, and

$$t_{\text{cross}} \approx 91 \text{ kyrs} \frac{(1 - e_{bd}^2)^{3/2}}{e_{bd}} \left(\frac{a_{bd}}{10.6 \text{ AU}} \right)^4 \times \left(\frac{M_{\star}}{M_{\odot}} \right)^{1/2} \left(\frac{16 M_{\text{Jup}}}{M_{bd}} \right) \left(\frac{1 \text{ AU}}{a_{\text{disk}}} \right)^{5/2} \quad (5)$$

for particles interior to the brown dwarf’s orbit, where the subscript ‘bd’ corresponds to the brown dwarf. The large mass of HD 206893 B drives t_{cross} at least two orders of magnitude shorter than t_{ss} , suggesting the observed debris belt is likely shaped by the brown dwarf. **Even after accounting for the uncertainties in both mass and eccentricity of the brown dwarf, its secular perturbation dominates over self-stirring (see blue band in Figure 5).** We note that the actual mass of the debris belt is not well constrained since the mass is dominated by large planetesimals (i.e., at the top of the collisional cascade) that are invisible. If the belt is more massive than the minimum mass solar nebula by at least two orders of magnitude, self-stirring can play a dominant role in replenishing the belt. There are reports of additional companions in the system including one massive companion interior to HD 206893 B (Grandjean et al. 2019) and another putative Jupiter-mass planet carving out the debris gap (Marino et al. 2020). **We note that the innermost companion, despite its mass, is too far away from the debris to have played a dominant role in sculpting the belts (the orbit crossing timescale**

1). For the brown dwarf mass, we assume the mass range $12\text{--}78 M_{\text{Jup}}$ derived in this work in Section 3.1. The wide chaotic zone also suggests a wide cavity around the orbit of the brown dwarf between ~ 2.4 and ~ 18.5 AU.

Next, we assess whether the observed debris belt is stirred by HD 206893 B. The debris belt could potentially be maintained by self-stirring, i.e., collision of ~ 1000 km-sized bodies at the top of the collisional cascade. Using Krivov & Booth (2018), we estimate the self-stirring timescale to be:

$$t_{ss,i} \sim 3.8 \text{ Myrs} \left(\frac{1.24 M_{\odot}}{M_{\star}} \right)^{0.35} \times \left(\frac{a_{\text{disk}}}{28 \text{ au}} \right)^{3.575} \left(\frac{\Delta a / a_{\text{disk}}}{0.73} \right)^{1.15} \quad (2)$$

within the belts due to the secular perturbation by the innermost companion is ~ 4 orders of magnitude longer than that by HD 206893 B calculated using 2.6 au, $15 M_{\text{Jup}}$, and $e = 0.02$). The putative Jupiter-mass planet inside the gap is more likely to be stirring the belts. Assuming $e = 0.02$, $0.9 M_{\text{Jup}}$, and 74 au, the orbit-crossing timescale is just as short as that due to HD 206893 B, but only for the outer belt. For this gap-opening planet to be a major stirrer of the inner belt, its eccentricity needs to be higher than ~ 0.2 . Our estimates are consistent with the analysis of Marino et al. (2020); see their Figure 10.

4. CONCLUSIONS

We detect the brown dwarf HD 206893 B in Ms-band with the Keck NIRC2 instrument and the vortex coronagraph (Serabyn et al. 2017) on 2018/09/24 with a signal-to-noise of 11. We measure its magnitude to be $M_s = 12.97_{-0.11}^{+0.10}$ and find its position is at an angular separation of 0.22 ± 0.03 arcsec, and a position angle (PA) of 39.6 ± 5.4 deg East of North. We use three evolutionary and atmospheric models (Baraffe et al. 2003; Allard et al. 2013; Chabrier et al. 2000), assume a distance of 40.77 pc (Gaia Collaboration 2020) and an age of 250_{-200}^{+450} Myr (Delorme et al. (2017)) to estimate the mass to be 12-78 M_{Jup} . We analyze the atmospheric properties of the brown dwarf from 1 to 5 microns using a grid of models appropriate to simulate brown dwarfs and exoplanet atmospheres (McKay et al. 1989; Marley et al. 1996; Marley & McKay 1999; Fortney et al. 2005, 2008; Saumon & Marley 2008; Morley et al. 2012). We find that an f_{sed} value ~ 0.2 provides the best fit to the data, suggesting high vertically extended clouds. This may be indicative of high altitude grains or a circumplanetary disk. We use evolutionary models (Saumon & Marley 2008) to find the best fitting masses and ages are $< 20 M_{\text{Jup}}$ and ages < 100 Myr, respectively. This is similar to the range derived by Delorme et al. (2017) and consistent with our estimates from the Ms-band photometry alone. We detect orbital motion of the brown dwarf around the host star in our 2018 data compared to the original 2015 and 2016 data (Milli et al. 2017; Delorme et al. 2017). We derive orbital parameters for the brown dwarf using the orbitize python package (Blunt et al. 2020; Foreman-Mackey et al. 2013). Finally we estimate the width of the chaotic zone of the brown dwarf companion in order to analyze how it interacts with the debris belt. We find that, due to the position and large mass of HD 206893 B, the debris belt is likely stirred by secular perturbation from the brown dwarf, rather than self-stirring of the planetessimals.

We thank the anonymous referee for their helpful suggestions that improved this paper. We thank our Keck/NIRC2 support staff, without whom the data could not have been obtained: Cynthia, Terry Stickel, Greg Doppmann, Bruno Femenía Castellá, and Carlos Alvarez. P. Gao and J. Wang acknowledge support from the 51 Pegasi b Fellowship sponsored by the Heising-Simons Foundation. P. Gao also supported by NASA through the NASA Hubble Fellowship grant HST-HF2-51456.001-A awarded by the Space Telescope Science In-

stitute, which is operated by the Association of Universities for Research in Astronomy, Inc., for NASA, under contract NAS5-26555. Part of this work has received funding from the European Research Council (ERC) under the European Union's Horizon 2020 research and innovation programme (grant agreement No 819155). This research has made use of the SVO Filter Profile Service (<http://svo2.cab.inta-csic.es/theory/fps/>) supported from the Spanish MINECO through grant AYA2017-84089. The plots presented in this paper were created using matplotlib in python (Hunter 2007). The data presented herein were obtained at the W.M. Keck Observatory, which is operated as a scientific partnership among the California Institute of Technology, the University of California and NASA. The Observatory was made possible by the generous financial support of the W.M. Keck Foundation. The Authors wish to recognize and acknowledge the very significant cultural role and reverence that the summit of Mauna Kea has always had within the indigenous Hawaiian community. We are most fortunate to have the opportunity to conduct observations from this mountain.

REFERENCES

- Ackerman, A. S., & Marley, M. S. 2001, ApJ, 556, 872
Allard, F. 2014, in IAU Symposium, Vol. 299, Exploring the Formation and Evolution of Planetary Systems, ed. M. Booth, B. C. Matthews, & J. R. Graham, 271–272
Allard, F., Homeier, D., Freytag, B., et al. 2013, Memorie della Societa Astronomica Italiana Supplementi, 24, 128
Amara, A., & Quanz, S. P. 2012, MNRAS, 427, 948
Baraffe, I., Chabrier, G., Barman, T. S., Allard, F., & Hauschildt, P. H. 2003, A&A, 402, 701
Baudino, J. L., Bézard, B., Boccaletti, A., et al. 2015, A&A, 582, A83
Blunt, S., Wang, J. J., Angelo, I., et al. 2020, AJ, 159, 89
Chabrier, G., Baraffe, I., Allard, F., & Hauschildt, P. 2000, ApJ, 542, 464
Charnay, B., Bézard, B., Baudino, J. L., et al. 2018, ApJ, 854, 172
David, T. J., Hillenbrand, L. A., Petigura, E. A., et al. 2016, Nature, 534, 658
Delorme, P., Schmidt, T., Bonnefoy, M., et al. 2017, A&A, 608, A79
Foreman-Mackey, D., Hogg, D. W., Lang, D., & Goodman, J. 2013, PASP, 125, 306
Fortney, J. J., Marley, M. S., Lodders, K., Saumon, D., & Freedman, R. 2005, ApJ, 627, L69
Fortney, J. J., Marley, M. S., Saumon, D., & Lodders, K. 2008, ApJ, 683, 1104
Gaia Collaboration. 2020, VizieR Online Data Catalog, I/350
Gomez Gonzalez, C. A., Wertz, O., Absil, O., et al. 2017, AJ, 154, 7
Grandjean, A., Lagrange, A. M., Beust, H., et al. 2019, A&A, 627, L9
Hiranaka, K., Cruz, K. L., Douglas, S. T., Marley, M. S., & Baldassare, V. F. 2016, ApJ, 830, 96
Huby, E., Bottom, M., Femenia, B., et al. 2017, A&A, 600, A46
Hunter, J. D. 2007, Computing in Science & Engineering, 9, 90
Konopacky, Q. M., Rameau, J., Duchêne, G., et al. 2016, ApJ, 829, L4
Krivov, A. V., & Booth, M. 2018, MNRAS, 479, 3300
Lew, B. W. P., Apai, D., Zhou, Y., et al. 2016, ApJL, 829, L32
Marino, S., Zurlo, A., Faramaz, V., et al. 2020, arXiv e-prints, arXiv:2010.12582
Marley, M. S., & McKay, C. P. 1999, Icarus, 138, 268
Marley, M. S., Saumon, D., Cushing, M., et al. 2012, ApJ, 754, 135
Marley, M. S., Saumon, D., & Goldblatt, C. 2010, ApJL, 723, L117
Marley, M. S., Saumon, D., Guillot, T., et al. 1996, Science (New York, N.Y.), 272, 1919

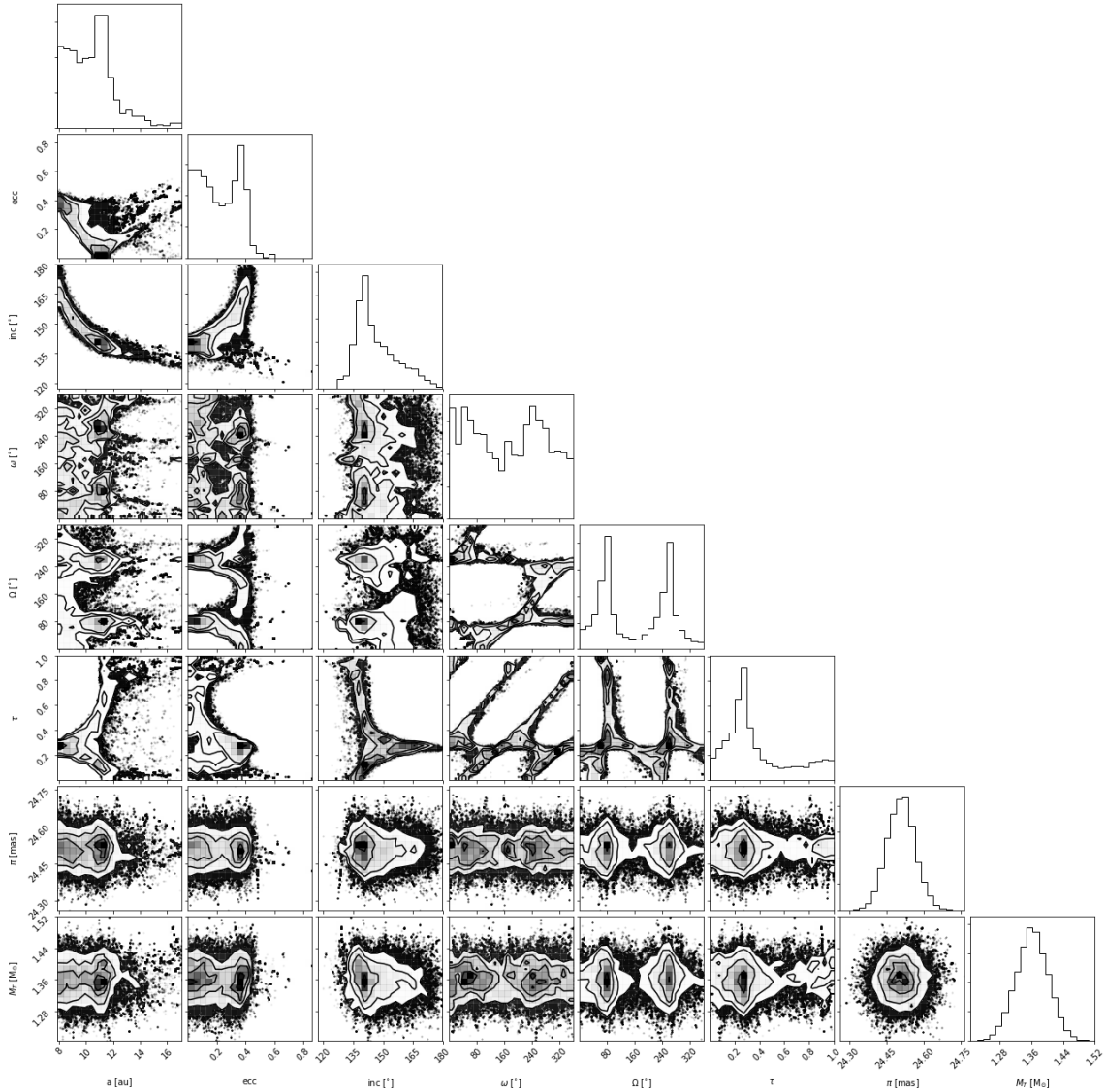


Figure 6. Posterior distributions for the orbital fit solution for HD 206893 B. The orbital parameters were derived using published astrometry (Milli et al. 2017; Delorme et al. 2017; Ward-Duong et al. 2020; Grandjean et al. 2019; Stolker et al. 2020) as well as the values derived in this work.

577 Marois, C., Lafrenière, D., Doyon, R., Macintosh, B., & Nadeau,
578 D. 2006, ApJ, 641, 556
579 Mawet, D., Milli, J., Wahhaj, Z., et al. 2014, ApJ, 792, 97
580 McKay, C. P., Pollack, J. B., & Courtin, R. 1989, Icarus, 80, 23
581 Milli, J., Hiben, P., Christiaens, V., et al. 2017, A&A, 597, L2
582 Moór, A., Abraham, P., Derekas, A., et al. 2006, ApJ, 644, 525
583 Morley, C. V., Fortney, J. J., Marley, M. S., et al. 2012, ApJ, 756,
584 172
585 Morrison, S., & Malhotra, R. 2015, ApJ, 799, 41
586 Mustill, A. J., & Wyatt, M. C. 2009, MNRAS, 399, 1403
587 Rajan, A., Rameau, J., De Rosa, R. J., et al. 2017, AJ, 154, 10
588 Rodrigo, C., & Solano, E. 2020, in Contributions to the XIV.0
589 Scientific Meeting (virtual) of the Spanish Astronomical
590 Society, 182

591 Rodrigo, C., Solano, E., & Bayo, A. 2012, SVO Filter Profile
592 Service Version 1.0, IVOA Working Draft 15 October 2012,
593 doi:10.5479/ADS/bib/2012ivoa.rept.1015R
594 Saumon, D., & Marley, M. S. 2008, ApJ, 689, 1327
595 Saumon, D., & Marley, M. S. 2008, ApJ, 689, 1327
596 Serabyn, E., Huby, E., Matthews, K., et al. 2017, AJ, 153, 43
597 Service, M., Lu, J. R., Campbell, R., et al. 2016, PASP, 128,
598 095004
599 Soummer, R., Pueyo, L., & Larkin, J. 2012, ApJL, 755, L28
600 Stephens, D. C., Leggett, S. K., Cushing, M. C., et al. 2009, ApJ,
601 702, 154
602 Stolker, T., Quanz, S. P., Todorov, K. O., et al. 2020, A&A, 635,
603 A182
604 Ward-Duong, K., Patience, J., Follette, K., et al. 2020, arXiv
605 e-prints, arXiv:2010.10546
606 Zakhochay, O. V., Zapatero Osorio, M. R., Béjar, V. J. S., &
607 Boehler, Y. 2017, MNRAS, 464, 1108
608 Zuckerman, B., & Song, I. 2004, ApJ, 603, 738